

# C1.2 Flow over the NACA0012 Airfoil

Takanori Haga<sup>1\*</sup>, Seiji Tsutsumi<sup>2\*</sup>, Ryoji Takaki<sup>3†\*</sup>, and Eiji Shima<sup>4\*</sup>

*\*Japan Aerospace Exploration Agency (JAXA), Sagamihara, Kanagawa, 252-5210, Japan*

*†Institute of Space and Astronautical Science (ISAS), Japan Aerospace Exploration Agency (JAXA), Sagamihara, Kanagawa, 252-5210, Japan*

## 1. Code description

- Discretization: The Navier-Stokes equations in the strong conservation form are discretized by the flux reconstruction (FR) scheme on unstructured hexahedral grids. The solution points (SP) are chosen to be Gauss quadrature points of a cell. To correct the flux polynomial,  $g_{Ga}$  polynomial function [1] is used.
- Relevant solvers: For shock capturing, a localized artificial diffusivity (LAD) scheme [2] is used. A simple WENO limiter [3] with TVB marker is also implemented. For time integration, a novel low storage defect correction on sub-cell (DECS) scheme is developed and used. The brief description of DECS is given in Sec. 2. The implicit block preconditioned LU-SGS [4] are also implemented.
- High-order capability: 2<sup>nd</sup> to 6<sup>th</sup> order schemes are implemented.
- Parallel capability: MPI/OpenMP hybrid parallelism is implemented for cluster machines of multicore architectures.
- Post-processing: For visualization, internal nodes within each cell are defined considering the degree of approximation polynomial. The solution variables at each internal node are reconstructed and stored. Fieldview, Tecplot and Plot3D (only for structured meshes) are supported. Turbulence statistics data and acoustic surface data for the FW-H solver are also supported.

## 2. Low storage defect correction on sub-cell (DECS) scheme

The DECS scheme constructs virtual sub-cells represented by the solution points within a cell. The sub-cell size is defined based on the Gauss quadrature weights for the corresponding solution point. The finite volume discretization is formulated for sub-cells with defining the flux and area vector at sub-cell interfaces. Implicit diagonal matrices in LHS of high-order FR discretization are roughly evaluated by the 1st-order FVM. For the simplified LHS, matrix free solver such as LU-SGS and MFGS can be used as is common for the FVM solvers. Therefore no extra memory storage is required for DECS. Due to the simplification, the convergence rate is slow in terms of the implicit time step. On the other hand, the computational cost for one implicit time step is small and in fact it is comparable with multi stage explicit Runge-Kutta scheme because expensive RHS evaluation is needed only once for each implicit step.

An inviscid subsonic flow over NACA 0012 is computed by the DECS and Block preconditioned LU-SGS (BLU-SGS) and the computational cost is compared. The freestream Mach number is 0.3 and the angle of attack is 0.5 degree. The convergence histories are shown in Fig. 1. The inner iteration for the linearized system is ten and three for DECS and BLU-SGS respectively. In terms of the time step, BLU-SGS shows faster convergence than DECS. In terms of the CPU time, however, DECS is faster than BLU-SGS expect for  $p=1$  approximation. For high order ( $p>1$ ) approximation, DECS is more efficient regarding the CPU cost and more importantly for the scale limiting memory storage.

## 3. Case summary

- Residual tolerances or other convergence criteria: 6 orders reduction in the residual norm of density.
- Machines used: Intel Xeon x5667 (3.07 GHz) CPU, 32 GB memory.
- Taubench CPU times on machines used (averaged for 10 times): 10.5409 [s]

---

<sup>1</sup> Aerospace Project Research Associate, JAXA, JEDI Center, [haga.takanori@jaxa.jp](mailto:haga.takanori@jaxa.jp).

<sup>2</sup> Engineer, JAXA, JEDI Center.

<sup>3</sup> Associate Professor, JAXA, ISAS/JEDI Center.

<sup>4</sup> Senior Researcher and Director, JAXA, JEDI Center.

- All the cases presented here (2D problems) are computed by the 3D hexahedral grid solver with one cell in the airfoil’s span direction. The definition of the “work unit” accounting for the increased cost is given in Sec. 4.B.

#### 4. Meshes

For this case, original O-type structured meshes were generated by an in-house pre-processing code. Five successively refined grids (80x20, 160x40, 320x80, 640x160, 1280x320) were generated. The finer grid is generated by increasing the boundary points on the airfoil and reducing the specified cell size at the leading and trailing edges and the wall distance. However, a finer grid was not generated recursively based on the coarser grid and the grid points are not exactly collocated between the grids. The far field is a circle and centered at the airfoil mid-chord with a radius of 1000 chords.

For the computations using more than  $p=1$  approximation polynomial, the curvature of the wing profile is reconstructed from the linear edge on the surface using the quadratic Bezier curves. One sided reconstruction is used at the trailing edge with sharp corner. For the computations using  $p=1$  approximation, linear grids are used.

#### 5. Results

Three different flow conditions are computed:

- Subsonic inviscid flow with  $M_\infty = 0.5$ , and angle of attack  $\alpha = 2^\circ$ .
- Transonic inviscid flow with  $M_\infty = 0.8$ , and  $\alpha = 1.25^\circ$ .
- Subsonic viscous flow with  $M_\infty = 0.5$ , and  $\alpha = 1^\circ$ , Reynolds number (based on the chord length)  $Re = 5,000$ .

Figure 2 shows the coarsest mesh (80x20). Mach number contours for the three flow conditions obtained by  $p=3$  approximation (4th-order) on 320x80 grid (1280x320 DOFs) are shown in Fig. 3-5.

##### A. Reference values for lift and drag coefficients

Grid convergence study for different  $p$  (1-4) was conducted on the four coarser grids. The reference lift and drag values are taken from the  $p=2$  solution on the finest grid (1280x320). It should be noted that the obtained values have not converged yet under the workshop criteria that is an error of 0.01 count. Although it is not shown here, reference values found in the prior workshop were also employed to compute the errors. However, we observed that the errors defined by the workshop reference values, in particular for the viscous case, did not converge consistently. The reference lift and drag coefficients used in this study are summarized in Table 1 with the convergence error (the difference from the values on the one-level coarser grid).

Table. 1. Reference values for lift and drag coefficients.

Case	$C_L$ (1280x320)	$ \Delta C_L $ Error	$C_D$ (1280x320)	$ \Delta C_D $ Error
Subsonic	2.864072E-1	0.000034	6.1004E-6	7.1674E-6
Transonic	3.513688E-1	0.000273	2.264974E-2	0.000058
Viscous	1.892E-2	0.00012	5.589E-2	0.00017

##### B. Estimate of work units

All computations start from a uniform freestream condition. To obtain a steady state solution, developed implicit DECS solver is employed. For subsonic inviscid and transonic inviscid flows, a steady state is declared if the density residual is reduced 6 orders of magnitude. For subsonic viscous flow, slower convergence was observed and a steady state is assumed if 5 orders residual reduction is obtained. These convergence criteria are used to calculate the work units. We note that the simulation is performed by in-house 3D code for hexahedral grids and the computational grids used in this study are 3D grids with one hexahedral cell in the spanwise direction. Considering there are  $p$  solution points in the spanwise direction, the wall-clock time for a 3D computation was divided by  $p$  to provide rough estimate for the work units. Therefore work units  $WU$  is computed by following equation:

$$WU = (T/p \cdot N)/T_{Tau} \quad (1)$$

where  $T$  is the wall-clock time,  $N$  is the number of cores used and  $T_{Tau}$  is the Taubench CPU time. In this study, all computations were performed using two cores of CPU via OpenMP thread parallelization ( $N = 2$ ).

### C. Results for subsonic inviscid flow

For the solution algorithm, newly developed low storage defect correction on sub-cell (DECS) scheme is used. The residual convergence histories in terms of the implicit time steps are summarized in Fig. 6. All computations converged to machine zero, though the convergence rate became slow down after 8 orders residual reduction. It is noted that favorable convergence trend with small dependency on  $p$  and  $h$  is observed.

The convergence of  $C_D$  and  $C_L$  errors in terms of the grid factor and work units are summarized in Fig. 7 and 8. High-order ( $p>1$ ) results show significantly small error comparing to the  $p=1$  (2nd-order) results. However, the convergence rate seems to be almost second order even though the flow is entirely smooth except for near the trailing edge. As pointed out by other workshop participants, controlling the error at TE to be not significant by using adaptive refinement will be necessary for achieving higher order convergence.

### D. Results for transonic inviscid flow

In this case, the LAD scheme [2] is employed for shock capturing with better steady state convergence. The residual histories in terms of the implicit time steps are summarized in Fig. 9. As is expected for a transonic flow condition with shock waves, the convergence rate is slower than the subsonic case. Nevertheless, enough convergence by reducing more than 6 orders of magnitude is obtained and superior convergence property of the LAD scheme is indicated. In fact, the simple WENO limiter [3] is also used for shock capturing instead of LAD, however the known convergence stall issue occurs as is the case using a polynomial reconstruction limiter. Again, it is noted that favorable convergence trend of small dependency on  $p$  and  $h$  is observed.

The convergence of  $C_D$  and  $C_L$  errors in terms of the grid factor and work units are summarized in Fig. 10 and 11. Comparing the lift errors,  $p=1$  results show smaller error than high-order computations. The reason for this is not clear and further investigation is undergoing. Meanwhile, high-order results show smaller drag error than  $p=1$  as is expected. It is noted that  $p=2$  and  $p=3$  results show competing performance in terms of the grid factor and also the work units. No clear benefit of higher order scheme seems to be reasonable since the flowfield is characterized by the shocks where only 1st order convergence is expected. However, it is desirable that the higher order solver can be applied to shock dominating flows without loss of robustness and efficiency, because it is not necessary to rely on involved  $h/p$  adaptive techniques especially for more complex flows with shock and turbulence interaction. The obtained convergence rates are almost second order as is the subsonic inviscid case.

### E. Results for subsonic viscous flow

The residual convergence histories in terms of the implicit time steps are summarized in Fig. 12. After the residual reduces 3-4 orders of magnitude, the convergence rate shows considerable slow down. The reason for the slower convergence is currently under investigation. In contrast to the inviscid flow cases, the convergence histories show notable  $p$  and  $h$  dependency.

The convergence of  $C_D$  and  $C_L$  errors in terms of the grid factor and work units are summarized in Fig. 13 and 14, respectively. High-order ( $p>1$ ) results show smaller lift and drag error comparing to the  $p=1$  (2nd-order) results. Comparing with drag errors, higher-order computations show faster convergence than second order.

## References

- (1) H.T. Huynh, "A flux reconstruction approach to high-order schemes including discontinuous Galerkin methods," AIAA Paper 2007-4079.
- (2) T. Haga, S. Kawai, "Toward accurate simulation of shockwave-turbulence interaction on unstructured meshes: a coupling of high-order FR and LAD schemes," AIAA Paper 2013-3065, 2013.
- (3) X. Zhong, C.W. Shu, "A simple weighted essentially nonoscillatory limiter for Funge-Kutta discontinuous Galerkin methods," *J. Comput. Phys.* 232 (2013), pp. 397-415.
- (4) T. Haga, K. Sawada and Z. J. Wang, "An implicit LU-SGS scheme for spectral volume method on unstructured tetrahedral grids," *Common. Comput. Phys.*, vol. 6, pp. 978-996, 2009.

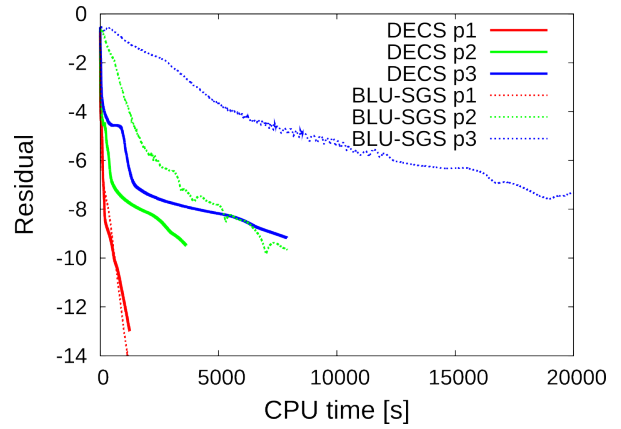
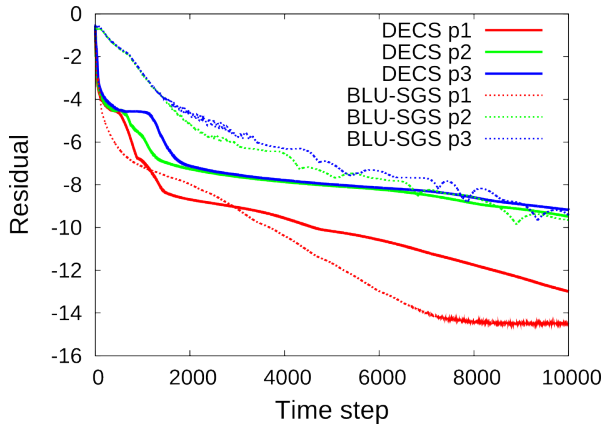


Fig. 1. Residual histories for inviscid subsonic flow over NACA 0012.

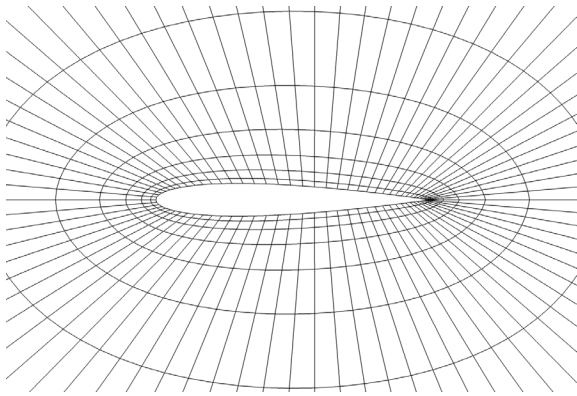


Fig. 2. Computational grid (the coarsest grid of 80x20 cells).

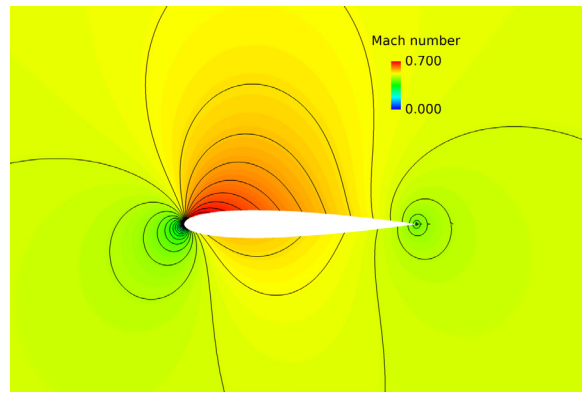


Fig. 3. Mach number contours for subsonic inviscid condition obtained by p=3 approximation with 320x80 grid.

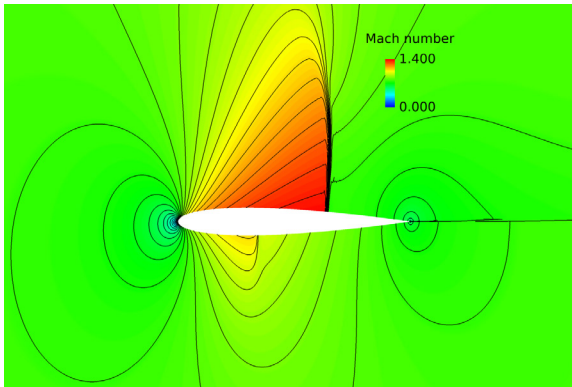


Fig. 4. Mach number contours for transonic inviscid condition obtained by p=3 approximation with 320x80 grid.

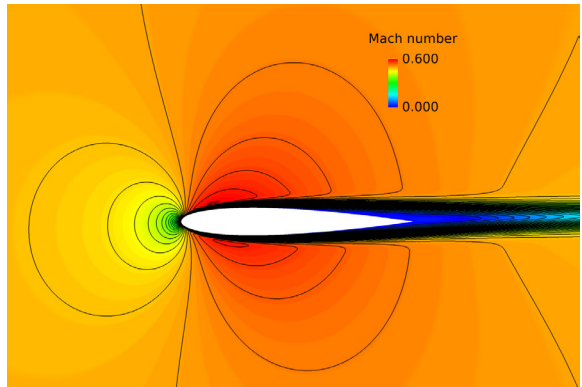


Fig. 5. Mach number contours for subsonic viscous condition obtained by p=3 approximation with 320x80 grid.

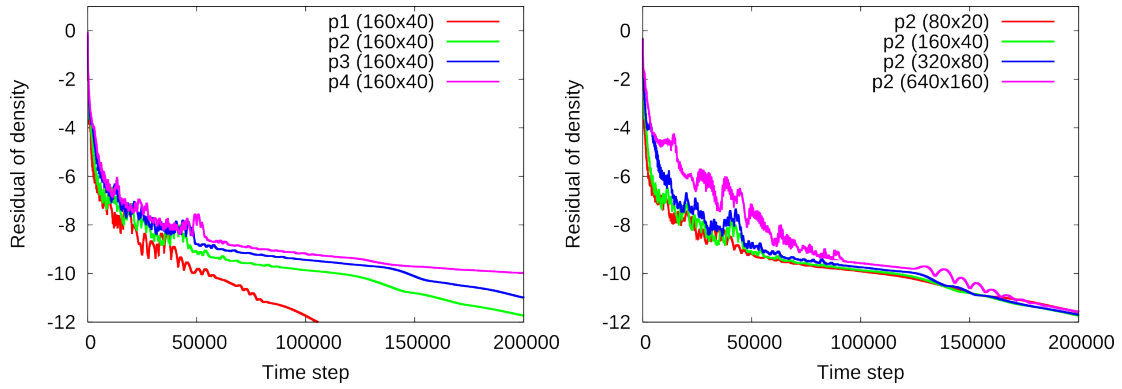


Fig. 6. Residual histories for subsonic inviscid flow condition. (Left for different  $p$  on a fixed mesh (160x40) and right for different grids with  $p=2$  for subsonic inviscid flow condition.

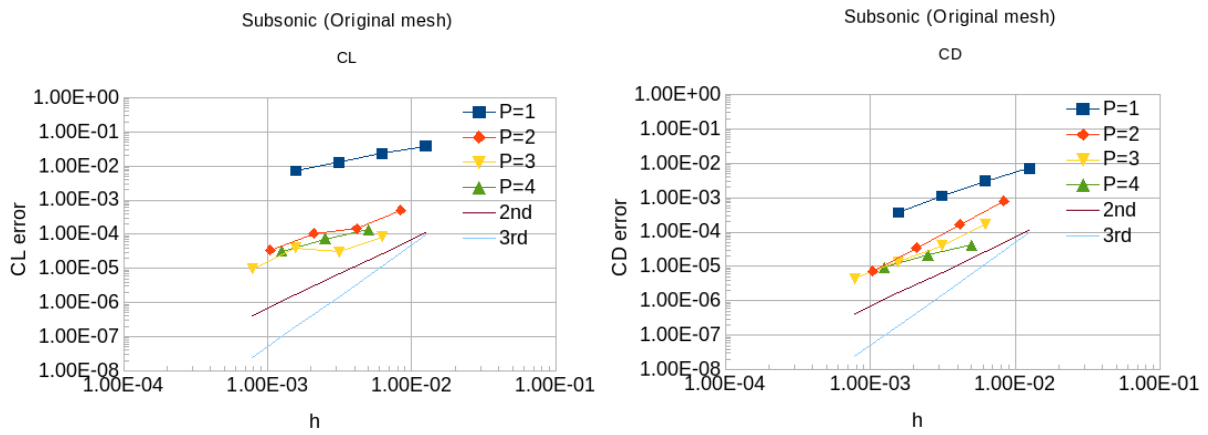


Fig. 7.  $C_D$  and  $C_L$  errors vs grid factor  $h$  for subsonic inviscid case.

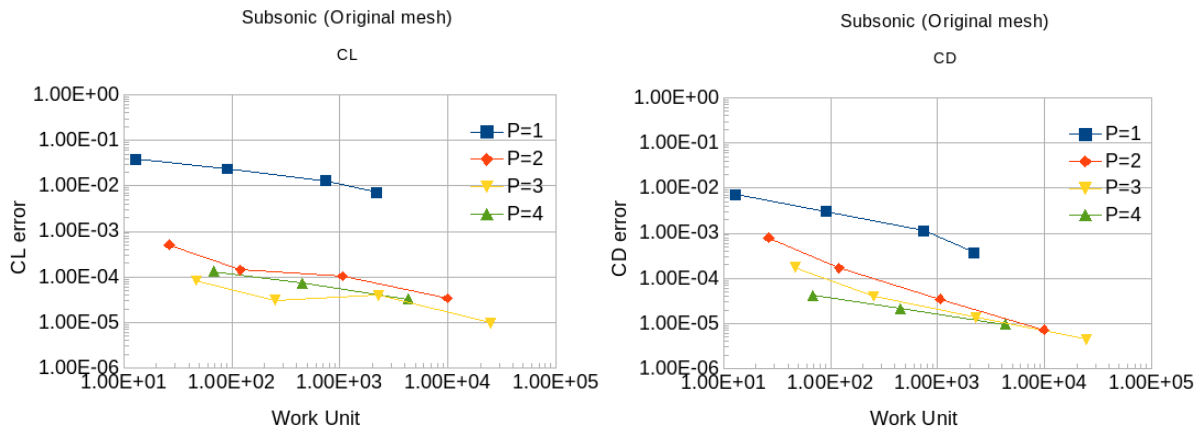


Fig. 8.  $C_D$  and  $C_L$  errors vs work units for subsonic inviscid case.

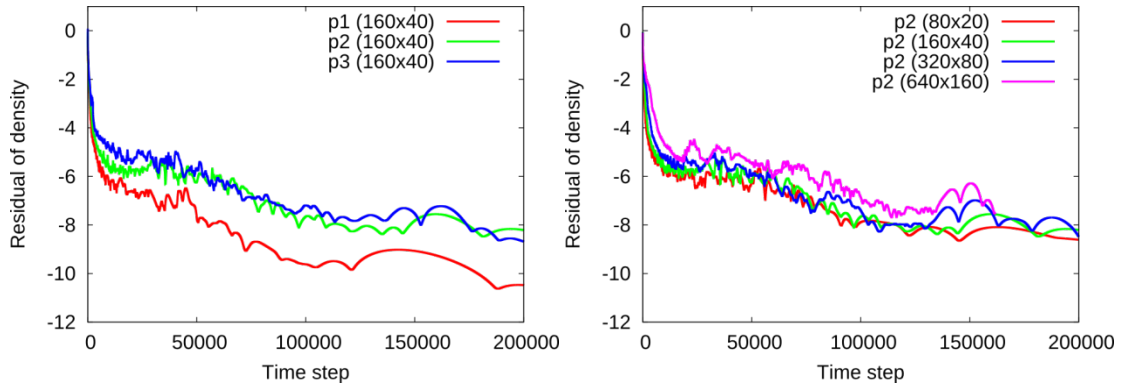


Fig. 9. Residual histories for transonic inviscid flow condition. (Left for different  $p$  on a fixed mesh (160x40) and right for different grids with  $p=2$  for subsonic inviscid flow condition.

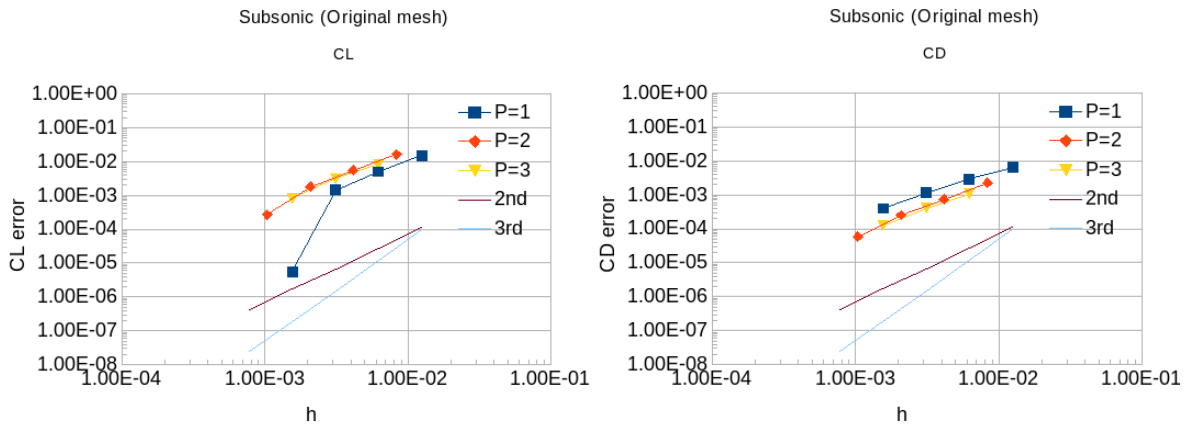


Fig. 10.  $C_D$  and  $C_L$  errors vs grid factor  $h$  for transonic inviscid case.

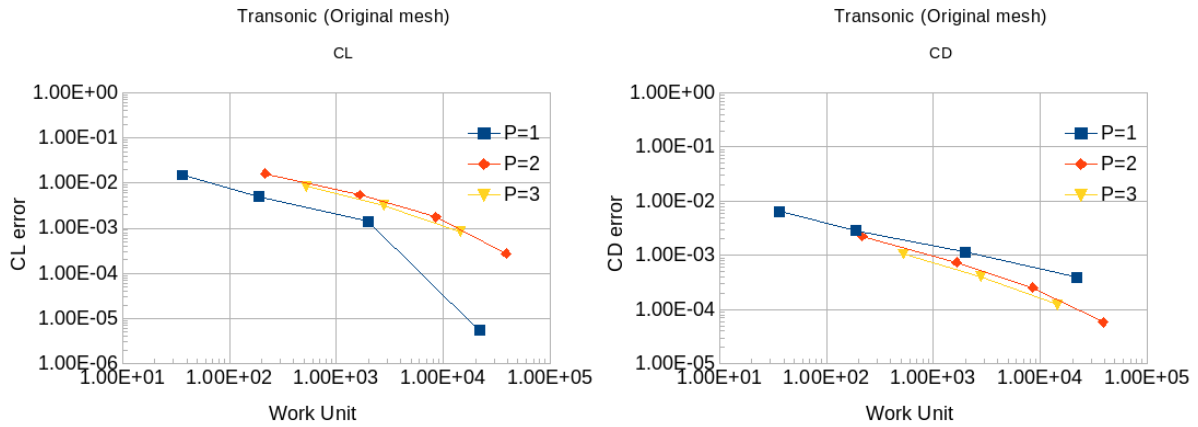


Fig. 11.  $C_D$  and  $C_L$  errors vs work units for transonic inviscid case.

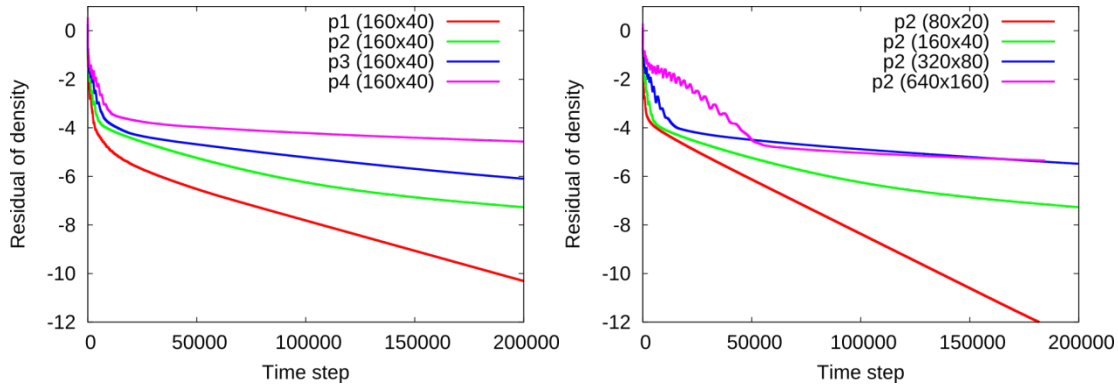


Fig. 12. Residual histories for subsonic viscous flow condition. (Left for different  $p$  on a fixed mesh (160x40) and right for different grids with  $p=2$  for subsonic inviscid flow condition).

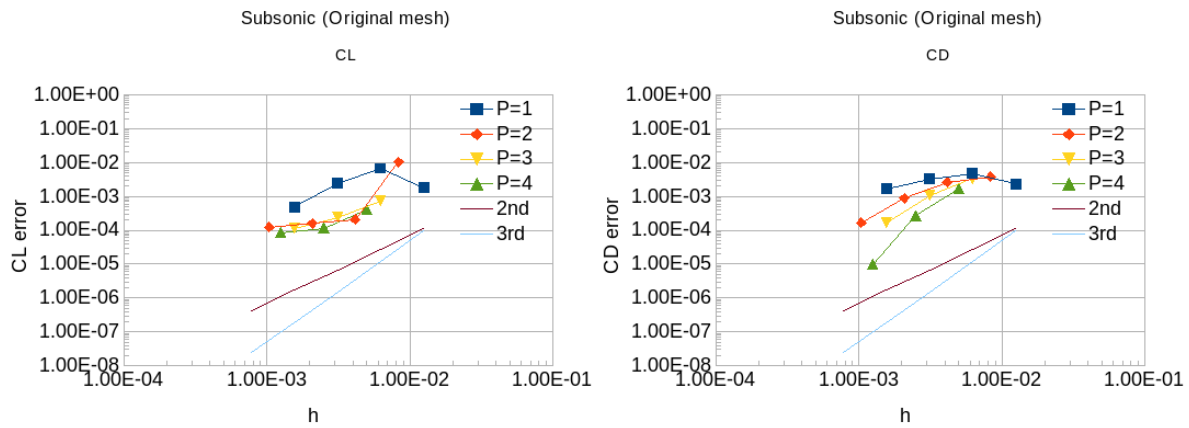


Fig. 13.  $C_D$  and  $C_L$  errors vs grid factor  $h$  for subsonic viscous case.

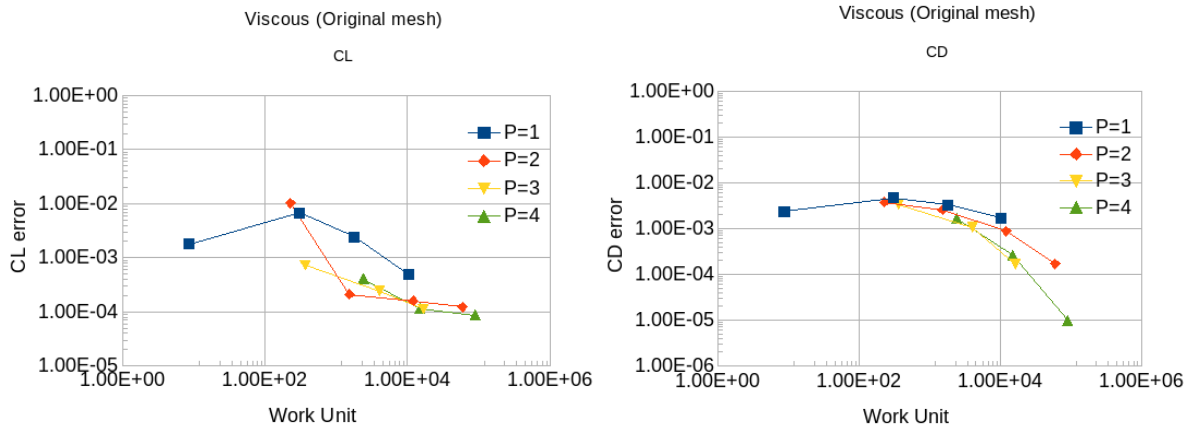


Fig. 14.  $C_D$  and  $C_L$  errors vs work units for subsonic viscous case.